IEEE Access
Multidisciplinary ⋮ Rapid Review ⋮ Open Access Journal

Received January 1, 2021, accepted January 12, 2021, date of publication February 1, 2021, date of current version February 12, 2021.

Digital Object Identifier 10.1109/ACCESS.2021.3056132

A Highly Sensitive Microwave Patch Sensor for Multidirectional Strain Sensing Based on Near Orthogonal Modes

LINGLING WANG[1], (Student Member, IEEE), KWOK L. CHUNG[1], (Senior Member, IEEE), WEIHUA ZONG[2], (Member, IEEE), AND BOTAO FENG[3], (Senior Member, IEEE)

[1]Civionics Research Laboratory, School of Civil Engineering, Qingdao University of Technology, Qingdao 266033, China
[2]School of Electronics and Information, Qingdao University, Qingdao 266071, China
[3]College of Electronics and Information Engineering, Shenzhen University, Shenzhen 518060, China

Corresponding authors: Botao Feng (fengbotao@szu.edu.cn) and Kwok L. Chung (klchung@qut.edu.cn)

This work was supported by the International Cooperation Research Foundation of Shenzhen (GJHZ20180418190621167) and the Shenzhen Fundamental Research Foundation (JCYJ20190808145013172).

ABSTRACT A passive wireless strain-sensing system for strain monitoring of metallic structures is presented in this paper, wherein single-feed (SF) patch antenna with near orthogonal fundamental modes is initiated as the sensing element. A new approach is proposed by using input admittance of the orthogonal modes as the strain measurand. Strain sensing proof-of-concept of the SF patch-sensor was first established through electromagnetic simulation, then a cantilever beam strain measurement system was designed and employed to quantify the changes of input admittance while directional strain was arising. The simulated results reinforced with mathematical derivation and verified by experimental results to demonstrate that there is a linear relationship between normalized admittance and micro-strain with a high sensitivity factor of 97 ppm/$\mu\varepsilon$ from simulation. Experimental results also verified that the single patch sensor can monitor the bidirectional (tensile and compressive) strain in multi-directions. An implementation example of the wireless passive sensing system is also presented in a proof-of-concept case. The change of minimum admittance that is linked with the applied strain was realized and interrogated using a monostatic radar system where the maximum radar cross section (RCS) and frequency differences were used as strain measurands. The interrogation method shows the RCS variations and the frequency shifts of the orthogonal modes in correspondence to the directional strains induced at the sensor in four uniaxial scenarios with a high sensitivity factor of 176 ppm/$\mu\varepsilon$.

INDEX TERMS Strain sensor, patch antenna, orthogonal modes, structural health monitoring, radar cross section (RCS).

I. INTRODUCTION

With the loading and environmental effect, the structural behavior will gradually degrade over time. Structural health monitoring (SHM) system has been extensively developed over the past decades to facilitate maintenance and reinforcement measures which utilize sensing systems to monitor and evaluate the state of structures [1]. Strain is one of the most important indicators in SHM, it directly reflects the state of damage that a structure is suffering from. For metallic structures, strain concentration is usually generated by high local stress which implies that a local void or cross-section shirking had occurred. Fluctuating stress and strain concentration can generate micro-cracks and will accelerate corrosion of metal structures. Once the crack spreads beyond the critical size and if not repaired in time, it may cause catastrophic failure [2]. In civil engineering, cracks can be detected by visual inspection with assistance of ultrasonic testing and binoculars [3]. However, manual inspection is labor intensive and time-consuming. SHM should be conducted preventively at a strain stage and not at a crack propagation stage, i.e. early detection, so that enough time can be spent on precaution and maintenance. Therefore, the possibility in monitoring the evolution of strain is of increasing interest in emerging SHM systems. Commercial strain sensors, such as metal foil strain gage, fiber Bragg grating sensor and vibrating string strain gauge

The associate editor coordinating the review of this manuscript and approving it for publication was Prakasam Periasamy.

have been widely implemented in engineering structures [4]–[9]. Metal foil strain gages are currently the most common solutions for strain monitoring due to their easy installation and low cost. Traditionally, common sensors are used in the SHM although significant improvements have been made on damage monitoring techniques by using advanced smart sensors. However, it cannot realize high *sensitivity factor* and wireless sensing demands to meet requirements of remote sensing or wireless sensor network. Moreover, it has low immunity to environmental factors such as temperature and humidity.

The Internet-of-Things (IoT) scenario, which provides data integration of monitoring, localization, classification and assessment, is becoming an attractive technology in SHM application. Wireless sensors network is also considered as a key of IoT in SHM application [10], [11]. Recently, a bridge monitoring radar with a central frequency of 36.05 GHz has been devised based on a millimeter-wave technology to measure the bridge vibration [12]. Antennas can be made passive and used as wireless sensors that can make the wireless SHM come true. In recent years, radio-frequency identification (RFID) technology is one of the alternative approaches for wireless sensing. Chipless RFID sensors have been proposed for strain sensing, corrosion prediction and crack detection [13]–[15]. A transducer is a device that converts energy from one physical quality to another one, such as a resonant frequency shift or a radar cross section (RCS) level fluctuation that is readily detectable by a remote radar system [16]. Thus far, various types of antenna-based strain sensors are based on linearly polarized (LP) patch antennas, using the relationship between fundamental resonant frequency and the *resonant length* of copper patch. A micro-fabricated patch antenna was designed for strain measurement [17]. For multi-direction detection, an LP circular-shaped patch antenna strain sensor was reported in [18]. Frequency doubling technique was adopted for antenna strain sensor [19], this approach can easily differentiate backscattered passive sensor signal from environmental electromagnetic reflections. RFID-based folded patch antenna was developed for strain sensing [20]–[22]. The advantage of these antenna sensors is wireless interrogation without a local power source. In order to study the effect of different substrates on transmission efficiency, a miniaturized quarter-wavelength microstrip patch antenna sensor was designed for simulation and experimental investigation [23]. Moreover, novel antenna sensors, which make use of resonant frequency shifts for detection and characterization of metallic surface crack, were investigated [24]–[26].

On one hand, wireless interrogation systems pay an important role for the effective remote sensing/detection as well as the overall system sensitivity factor. Conventionally, both the monostatic [27]–[29] and bistatic [30]–[32] radar or RFID systems have been widely used. In [27], a monostatic interrogation was used to capture the frequency shift from a large RF cavity sensor, whereas a frequency modulated continuous wave (FMCW) radar was used in [28] for real-time vibratory strain sensing. Time-domain gating-based interrogations were commonly employed in different systems for wireless temperature sensing [29]–[31], where local temperature changes were reflected by the frequency shifts in the remote ends. In [31] and [32], tailor made ultra-wideband (UWB) antennas were used as transmitting and receiving antennas in bistatic systems, where short interrogation ranges were reported. On the other hand, a high sensitivity factor of sensing element is highly desired.

For those LP patch antenna-based strain sensors mentioned above, the sensing parameter was based on single (either TM10 or TM01) mode's resonant frequency shifts with strain increasing. Unfortunately, the LP patch antenna is insensitive to the patch width changes, thereby this method of LP-patch merely contributes one-dimensional strain monitoring with a maximum sensitivity factor of 1 ppm/$\mu\varepsilon$ [24]. This is mainly due to the fundamental resonant frequency of the LP-patch antenna which depends on the value of patch length rather than the width. Recently, a novel design of RF strain transducer based on a LP-patch antenna loaded with open-loop resonators was proposed for high-sensitive sensing of two-dimensional (2-D) strains. The prototypes achieved a maximum sensitivity (factor) of 2.35 ppm/$\mu\varepsilon$ [16]. This dual-element method offers sensitivity value that improves the LP patch sensors; it is still found to be low and may not be suitable for high sensitivity factor demands. This has motivated us to create a single sensing element that is capable of multi-directional strain sensing with a high gauge factor.

A sensor of single-feed circularly polarized (SFCP) patch based on orthogonal mode was first initiated by the authors [33], where we presented a comparative study into the directional sensitivity factor of two coaxial probe-fed LP-patch sensors and CP patch. The physical configurations between CP- and LP-patch were maintained to be the same except the feed positions. Strain sensing parameters of LP patch can only be based on single mode's resonant frequency shifts, whereas the CP-patch generates simultaneously two radiation modes. This CP-patch sensor exhibits at least 55 times more sensitive than the LP-patch counterpart by the proof-of-concept prototype [33]. In this paper, we further extended our studies from the probe-feed to microstrip-line feed patch sensor, where the microstrip-line is integrated with the strain sensor as a whole so that artificial hole is not required to accommodate the coaxial feed on the metallic structures in order to fulfill the integrity of structure. A SFCP antenna-based strain sensor for the aim of monitoring multidirectional tensile and compressive strains with an ultra-high sensitivity factor is presented. The innovative idea presented here is to make use of the orthogonal fundamental modes (TM01 and TM10) where their resonant frequencies are tuned next to each other. A new sensing method is also proposed in which we used the input impedance/admittance of the CP patch antenna as the strain-sensing characteristics for monitoring the 2-D deformation. For an attempt of investigation, input admittance of CP-patch at different strain levels for x- and y-direction were analyzed. Minima of admittance between two

orthogonal modes were examined to be shifted as a linear function of micro-strain. The predicted results, verified with the experiment, demonstrated that high sensitivity factors of 97 and –99 ppm/$\mu\varepsilon$ for x- and y-direction strain, respectively, were achieved. Moreover, an implementation example of the wireless passive sensing system is demonstrated as a proof-of-concept configuration. The CP-patch sensor was realized and interrogated using a monostatic FMCW radar system, where its radar cross section (RCS) feature was extracted to quantify the admittance/impedance-strain variations. The interrogation method shows that very high sensitivity factors (–66 and 92 ppm/$\mu\varepsilon$) were obtained on the changes of maximum RCS as well as the difference of mode-frequencies (–175 and 118 ppm/$\mu\varepsilon$) with respect to the directional strains induced at the sensor. The practical novelty and contributions of this article can be summarized as follows:

i) theoretical derivation is justified for the feasible use of patch-sensor with near orthogonal modes;
ii) multidirectional strain is realized by using a single sensing element;
iii) achieved ultra-high sensitivities under wire and wireless (RCS) scenarios are demonstrated;
iv) relations on the input impedance, surface currents of CP-patch and the complex RCS under various strains are examined.

The rest of this paper is organized as follows. Section II presents the operation principle of strain sensing. Section III describes the design and numerical simulation of the CP-patch sensor. Sections IV and V demonstrate, respectively, the experimental verifications on the CP-patch sensor and an example of passive remote sensing system using the CP-patch sensor, where the variations of RCS behave as a function of directional strain. Finally, a conclusion is drawn in Section VI.

II. PRINCIPLE OF OPERATION FOR STRAIN SENSING

The copper patch and the ground plane form a microwave resonant cavity based on the cavity-model theory. Typically, a SFCP nearly-square patch antenna generates simultaneously two fundamental modes: TM01 mode and TM10 mode. The TM10 mode indicates that the electric field is parallel to the geometric longitudinal direction, whereas the TM01 mode is polarized along its width direction. Figs. 1(a) and 1(b) show the ideal equivalent circuits of the microstrip-line fed nearly-square patch antenna (see Fig. 2). For the sake of clarity, hereunder we use Mode A and Mode B to denote TM10 and TM01, respectively.

The input impedance of the CP antenna with two degenerative modes is derived from the equivalent circuit analysis. Two parallel-connected circuits with resistor (R), capacitor (C) and inductor (L) correspond to the two orthogonal modes of the patch resonator, where R_X represents the radiation resistances; C_X and L_X represent the energy-storage elements of two modes: capacitors and inductors of the patch resonator,

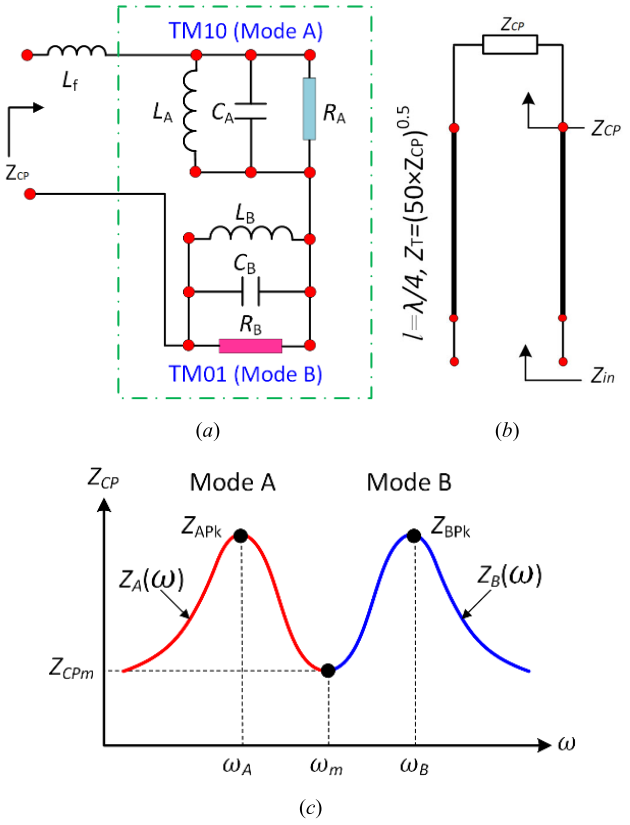

FIGURE 1. Equivalent circuits of CP patch antenna-based strain sensor: (a) corner-fed nearly-square patch antenna, (b) microstrip-line feed with quarter-wave impedance matching network, (c) variation of input impedance (Z_{CP}) as a function of frequency (ω).

whereas L_f represents the feed inductance. Z_{CP}, Z_T, Z_{in} are, respectively, the input impedance of the CP patch, characteristic impedance of the quarter-wave transformer, and the overall input impedance/admittance. The input impedance of the CP patch and the overall input admittance in complex forms are given by

$$\begin{aligned} \boldsymbol{Z_{CP}}(\omega) &= j\omega L_f + \mathbf{Z_A}(\omega) + \mathbf{Z_B}(\omega) \\ &= j\omega L_f + 1/\left(j\omega C_A + 1/R_A + 1/j\omega L_A\right) \\ &\quad + 1/\left(j\omega C_B + 1/R_B + 1/j\omega L_B\right) \end{aligned} \tag{1}$$

$$\boldsymbol{Y_{in}}(\omega) = \frac{1}{\boldsymbol{Z_{in}}(\omega)} = \frac{\boldsymbol{Z_{CP}}(\omega)}{Z_T(\omega)^2} \tag{2}$$

Unlike conventional LP-patch strain sensors, which use the changes of resonant frequency as a function of micro-strain [15], [21]–[25], the uniaxial strains along the principle axes can be monitored simultaneously using a number of sensing variables. Namely, the design of the new strain sensor relies on the dual resonant frequency (ω_A, ω_B), maxima (Z_{APk}, Z_{BPk}) and minimum (Z_{CPm}) of input impedance as a function of strain, which are the consequences of the changes of R_X, C_X and L_X. Neglecting the feed inductance (L_f) due to the fact that a very thin substrate is used, Fig. 1(c) displays the input impedance of the orthogonal modes from an *ideal* SFCP patch antenna, where its maxima are equaled whereas Z_{CPm}

occurs at ω_{m} with ω_{B}–$\omega_{\mathrm{m}} = \omega_{\mathrm{m}}$–$\omega_{\mathrm{A}}$, and hence the modulus of the input impedance (1) can be expressed as

$$Z_{CPm} = Z_A(\omega_m) = Z_B(\omega_m) \tag{3a}$$
$$= \left|1\Big/\left(1/R_{\mathrm{B}} + j\left(\omega C_{\mathrm{B}} - 1/\omega L_{\mathrm{B}}\right)\right)\right| \tag{3b}$$
$$= \left[R_B^{-2} + \left(\omega_m C_B - \frac{1}{\omega_m L_B}\right)^2\right]^{-1/2} \tag{3c}$$

The resonant frequencies of Mode A and Mode B are related to the patch length (A) and patch width (B), respectively, as

$$\omega_A = \frac{\pi c}{A\sqrt{\kappa_r}}, \quad \omega_B = \frac{\pi c}{B\sqrt{\kappa_r}} \tag{4a), (4b)}$$

and

$$\omega_m = \frac{1}{2}\frac{\pi c\,(A+B)}{AB\sqrt{\kappa_{\mathrm{r}}}} \tag{4c}$$

where $c = 1/\sqrt{\kappa_0\mu_0}$ is the velocity of light, κ_0 and μ_0 are the free-space permittivity and permeability, respectively; κ_{r} is the relative dielectric constant of the dielectric substrate.

Considering the uniaxial strain arose along x-axis, the electrical circuit elements of Mode B have their relations with the CP-patch's physical parameters as given by [34],

$$C_B = \kappa_0\kappa_{\mathrm{r}}AB/h, \tag{5a}$$
$$L_B = \frac{u_0 hB}{\pi^2 A}, \tag{5b}$$
$$R_B = \frac{Q_T}{\omega_B C_B} = \frac{\sqrt{\kappa}_{\mathrm{r}}B}{2\pi c\kappa_0 A}, \tag{5c}$$

where Q_{T} is the total quality factor of the patch resonator, which is approximated by $Q_T \approx \frac{\pi c\sqrt{\kappa_{\mathrm{r}}}}{2\omega_{\mathrm{B}}h}$.

We take the partial derivatives for (3c),

$$\frac{\partial Z_{CPm}}{\partial R_B} = \frac{Z_{CPm}^3}{R_B^3} = G_R(B)\frac{Z_{CPm}}{R_B}, \tag{6a}$$
$$\frac{\partial Z_{CPm}}{\partial C_B} = \frac{1-\omega_m^2 C_B L_B}{L_B} Z_{CPm}^3 = G_C(B)\frac{Z_{CPm}}{C_B}, \tag{6b}$$
$$\frac{\partial Z_{CPm}}{\partial L_B} = \frac{1-\omega_m^2 C_B L_B}{\omega_m^2 L_B^3} Z_{CPm}^3 = G_L(B)\frac{Z_{CPm}}{L_B}, \tag{6c}$$
$$\frac{\partial Z_{CPm}}{\partial \omega_m} = \frac{1-\omega_m^4 C_B^2 L_B^2}{\omega_m^2 L_B^2} = G_\omega(B)\frac{Z_{CPm}}{\omega_m}, \tag{6d}$$

where $G_{\mathrm{R}}(B)$, $G_{\mathrm{C}}(B)$, $G_{\mathrm{L}}(B)$ and $G_\omega(B)$ are the functions of patch width B and physical parameters (constants).

The variations of the input impedance can be expressed in terms of four differential changes from (3c), as given by

$$\delta Z_{CP_m} = \frac{\partial Z_{CP_m}}{\partial R_B}\delta R_B + \frac{\partial Z_{CP_m}}{\partial C_B}\delta C_B + \frac{\partial Z_{CP_m}}{\partial L_B}\delta L_B + \frac{\partial Z_{CP_m}}{\partial \omega_m}\delta\omega_m \tag{7}$$

Substituting (6) into (7) and taking normalization, yields

$$\frac{\delta Z_{CP_m}}{Z_{CPm}} = G_R(B)\frac{\delta R_B}{R_B} + G_C(B)\frac{\delta C_B}{C_B} + G_L(B)\frac{\delta L_B}{L_B} + G_\omega(B)\frac{\delta\omega_m}{\omega_m} \tag{8}$$

Let δR_{B}, δC_{B}, δL_{B} and $\delta\omega_{\mathrm{m}}$ be the small changes of R_{B}, C_{B}, L_{B} and ω_{m}, respectively, due to the small change on patch width δB when *x-direction strain* occurs. By taking the natural logarithm on both sides of (4c) and (5), we obtain

$$\ln(\omega_m) = \ln\left(\frac{1}{2}\frac{\pi c\,(A+B)}{AB\sqrt{\kappa_{\mathrm{r}}}}\right), \tag{9a}$$
$$\ln(C_B) = \ln(\kappa_0\kappa_{\mathrm{r}}AB/h), \tag{9b}$$
$$\ln(L_B) = \ln\left(\frac{u_0 hB}{\pi^2 A}\right), \tag{9c}$$
$$\ln(R_B) = \ln\left(\frac{\sqrt{\kappa}_{\mathrm{r}}B}{2\pi c\kappa_0 A}\right). \tag{9d}$$

Taking derivative on both sides of (9a) to (9d) with respect to B, yields

$$\frac{1}{\omega_m}\frac{\delta\omega_m}{\delta B} = \frac{2AB\sqrt{\kappa_{\mathrm{r}}}}{\pi c\,(A+B)}\frac{2\pi cAB\sqrt{\kappa_{\mathrm{r}}} - 2\pi c\,(A+B)A\sqrt{\kappa_{\mathrm{r}}}}{4A^2B^2\kappa_{\mathrm{r}}}, \tag{10a}$$
$$\frac{1}{C_B}\frac{\delta C_B}{\delta B} = \frac{h}{\kappa_0\kappa_{\mathrm{r}}AB}\frac{\kappa_0\kappa_{\mathrm{r}}A}{h}, \tag{10b}$$
$$\frac{1}{L_B}\frac{\delta L_B}{\delta B} = \frac{\pi^2 A}{u_0 hB}\frac{u_0 h}{\pi^2 A}, \tag{10c}$$
$$\frac{1}{R_B}\frac{\delta R_B}{\delta B} = \frac{2\pi c\kappa_0 A}{\sqrt{\kappa}_{\mathrm{r}}B}\frac{\sqrt{\kappa}_{\mathrm{r}}}{2\pi c\kappa_0 A}, \tag{10d}$$

Further simplify (10a) to (10d), we have

$$\frac{\delta\omega_m}{\omega_m} = -\frac{A}{A+B}\frac{\delta B}{B}, \tag{11a}$$
$$\frac{\delta C_B}{C_B} = \frac{\delta B}{B}, \tag{11b}$$
$$\frac{\delta L_B}{L_B} = \frac{\delta B}{B}, \tag{11c}$$
$$\frac{\delta R_B}{R_B} = \frac{\delta B}{B} \tag{11d}$$

Assuming the uniaxial strain along x-axis, $\varepsilon_{\mathrm{X}}\left(\stackrel{\mathrm{def}}{=} \delta B/B\right)$, is sufficiently small causing the differential changes with $\delta C_{\mathrm{B}} \ll C_{\mathrm{B}}$, $\delta L_{\mathrm{B}} \ll L_{\mathrm{B}}$, $\delta R_{\mathrm{B}} \ll R_{\mathrm{B}}$ and $\delta\omega_{\mathrm{m}} \ll \omega_{\mathrm{m}}$. When $\delta B \to 0$, $B \approx B_0$, equation (8) can be expressed in terms of ε_{X} as

$$\frac{\delta Z_{CP_m}}{Z_{CPm}} = \lim_{\delta B\to 0}\left(G_R(B) + G_C(B) + G_L(B) + H_\omega(B)\right)\frac{\delta B}{B} \tag{12a}$$
$$\cong \left(G_R(B_0) + G_C(B_0) + G_L(B_0) + H_\omega(B_0)\right)\varepsilon_{\mathrm{X}} \tag{12b}$$

where $H_\omega(B_0) = -A/(A+B_0)G_\omega(B_0)$, and all functions are constants.

Finally, solving (2) and (12), yields

$$\frac{\delta Y_{min}}{Y_{min}} = \frac{Z_T^2}{Z_T^2}\frac{\delta Z_{CP_m}}{Z_{CPm}} = K_{\mathrm{X}}\varepsilon_{\mathrm{X}} \tag{13}$$

where K_{X} is the strain sensitivity factor for the x-direction strain.

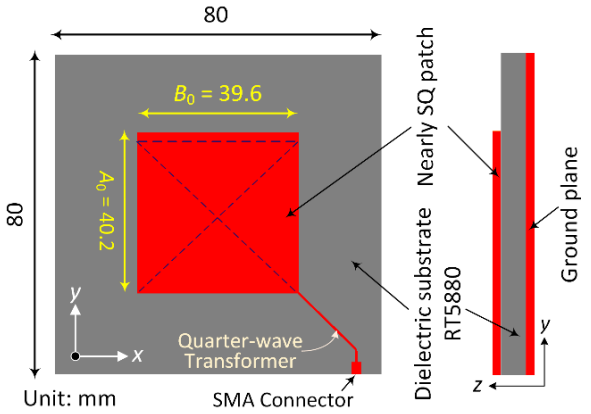

FIGURE 2. Top- and side-view of CP-patch-based strain sensor.

In the same manner, the stain sensitivity factor K_Y can be derived via electrical components of Mode A when the *y-direction strain* ($\varepsilon_Y \overset{\text{def}}{=} \delta A/A$) occurs.

III. DESIGN AND SIMULATION OF CP-PATCH SENSOR

A. GEOMETRY OF THE CP-PATCH SENSOR

The proposed CP-patch strain monitoring sensor composed of a microstrip-line fed nearly square copper foil/patch and a ground plane printed on the top- and bottom-side of a dielectric substrate, as shown in Fig. 2. The nearly square patch has a physical size of A and B. A perturbation segment of $(A–B) \times B$ was included on the square patch such that the two near-orthogonal modes, TM01 and TM10, meet the necessary conditions for the generation of circular polarization in the broadside direction.

B. STRAIN MODELLING OF THE CP-PATCH

In order to acquire an accurate prediction about the performance of the CP antenna-based sensor for strain monitoring, a simulation model of the nearly-square patch antenna was established by using CST Microwave Studio. The strain propagation was simulated by applying size change of copper patch under the hypothesis that the dielectric constant and its copper ground-plane have no effect on their values due to the tangential strain. The RT/duroid® 5880 with a thickness (h) of 0.787 mm was selected as the dielectric substrate for its suitable elastic modulus (∼965 MPa) and low dielectric constant and dielectric loss ($\kappa_r = 2.2$, $\tan\delta = 0.001$). After the EM simulation of antenna in the initial state (under 0 $\mu\varepsilon$), a good CP performance of the patch antenna was obtained. Then, the tensile and compressive strain application in x- and y-direction were simulated by increasing and decreasing initial patch width (B_0) and length (A_0), respectively. To prevent material deformation during strain application, the variation range of patch size was set from −0.056 to +0.056 mm in a strain-calculated (equivalent) step of 0.014 mm. For the x-direction deforming model, nine strain levels (−1414.1 to +1414.1 $\mu\varepsilon$ at an equivalent step of 353.5 $\mu\varepsilon$) were applied. For the y-direction deforming model, another nine strain levels were used, namely, from −1393.0 to 1393.0 $\mu\varepsilon$ at an equivalent step of 348.3 $\mu\varepsilon$. In order to take the Poisson effect of copper patch into account during elongation or compression, both the patch length and width have to be changed simultaneously. For x-direction strain, the width is changed due to the force applied whereas the length is also changed due to the Poisson effect of copper, as calculated by

$$B = B_0\,(1 + \varepsilon_X), \tag{14a}$$
$$A = A_0(1 - \nu\varepsilon_X). \tag{14b}$$

Likewise, for the y-direction strain

$$A = A_0\,(1 + \varepsilon_Y) \tag{14c}$$
$$B = B_0(1 - \nu\varepsilon_Y) \tag{14d}$$

where ε_X and ε_Y can be positive or negative; a positive value indicates a tensile strain whereas a negative value represents a compressive strain; ν is a positive number representing the Poisson's ratio of the copper patch (typically 0.34).

C. SIMULATION RESULTS FOR DIRECTIONAL STRAIN SENSING

The input admittance of CP-patch sensor with four orthogonal directions were computed and the results versus frequency are shown in Fig. 3, wherein the maxima and minima of admittance curves under different directional strain levels are studied. When the *x-direction* tensile strain increases (ε-XP↑), the admittance of TM01 mode was observed to shift to the left whereas the admittance of TM10 mode was almost maintained, as shown in Fig. 3(a). In the same figure, a consistent right shift of maximum admittance of TM01 mode was observed while the compressive strain was increasing (ε-XN↑). As a result, the admittance change of TM01 mode can be regarded as an indicator for the monitoring of *x-direction* strain, whereas the movement directions of minima (between two modes) can be used as a distinction to judge the compressive or tensile strain.

Likewise, there are obvious left shifts of maxima of TM10 mode under tensile strain along *y-direction*, whereas right shifts of maxima of TM10 mode under compressive strain were observed as shown in Fig. 3(b). Again, opposite directions of minima appeared for the increments of compressive (ε-YN↑) and tensile (ε-YP↑) strains.

IV. EXPERIMENTAL VERIFICATIONS

A. FABRICATION OF ANTENNA SENSOR

The proposed CP-patch strain sensor was implemented by using dielectric laminate RT/duroid® 5880 with a thickness of 0.787 mm. The copper ground-plane of the CP-patch strain sensor was bonded with the aluminum cantilever-beam with superglue. The fabricated prototypes of aluminum beam-specimens are shown in Fig. 4.

Before exerting directional strains on the sensors, we compared the simulated and measured input admittance, as shown in Fig. 5. The input admittance of the SFCP antenna sensors was measured by a Keysight Performance Network

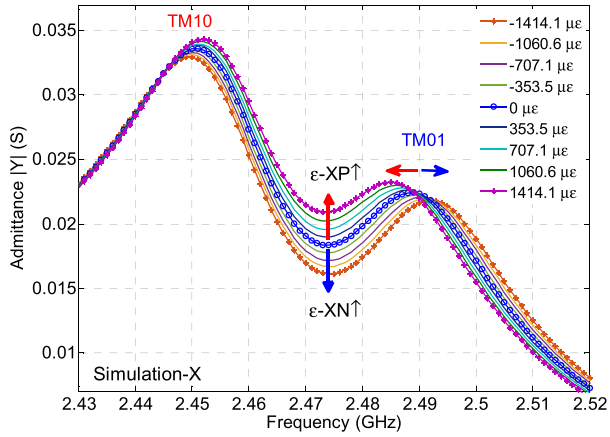

(a)

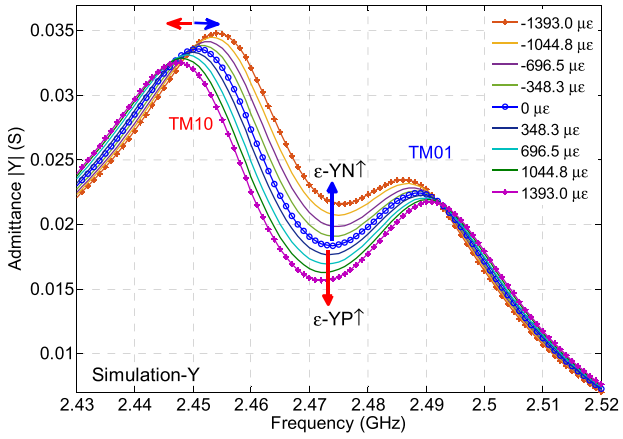

(b)

FIGURE 3. Variation of input admittance |Y| under four scenarios: (a) x-direction tensile and compressive strain, (b) y-direction tensile and compressive strain.

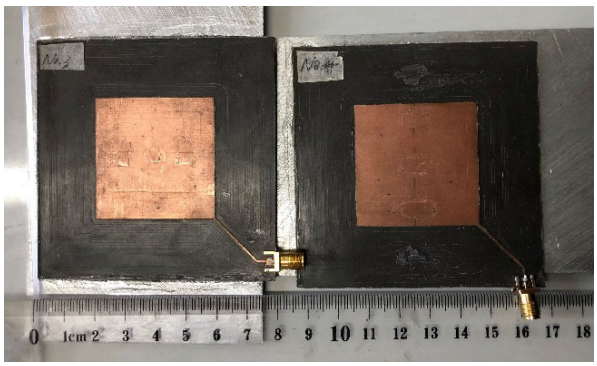

FIGURE 4. Photographs of the fabricated patch sensors.

Analyzer (PNA, N5222A) after calibration. The slight mismatch between the simulated with measured admittance was observed, which may be contributed by the fabrication and material uncertainties. However, this will not affect the sensor's practical performance as the changes of input admittance will be computed with respect to the measured reference status.

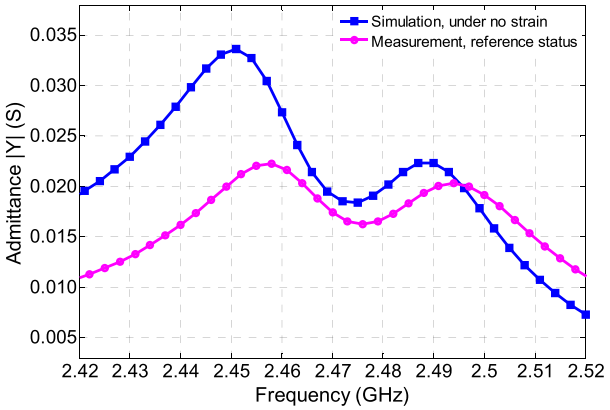

FIGURE 5. Measured and simulated input admittance.

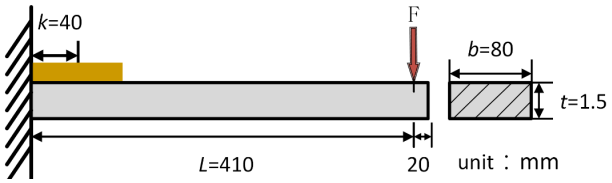

FIGURE 6. Cross sectional view of the cantilever beam.

B. EXPERIMENTAL SETUP OF CANTILEVER BEAM SYSTEM

For measuring the admittance response of the CP-patch sensor under different strain levels, a cantilever beam made by AL1060 aluminum (GB/T3190-1996) was designed to validate the utilization of proposed strain sensor. The aluminum cantilever specimen has an overall length of 450 mm composed of a clamping position (20 mm), loading distance (20 mm) and a beam length (410 mm) as illustrated in Fig. 6. The position of sensors, which were connected to both surfaces of the cantilever beam using superglue (Fig. 4 and Fig. 7), was determined by occurrence of the largest strain. As such, this adhesive method allows transmission of aluminum strain to CP-patch sensors. In order to assess the effect of strain direction along both x- and y-direction on the input admittance, the patch sensors can be elongated and shortened along these two directions. Hence, two types of microstrip-line feed patch sensor were deliberately devised, where the feed-lines are symmetrical along the 45°-diagonal line (Fig. 4). The patch sensors bonded on the top- and bottom-side were placed in the same distance from the free end on opposite sides of cantilever beam in order to obtain accurate directional strain levels.

The weights were applied at the free end and thus generated a moment. Based on the elastic flexure theory and Hooks Law, the directional micro-strain ε_k experienced by the patch sensor at position k can be expressed by

$$\varepsilon_k = \frac{6\boldsymbol{F}(L-k)}{E_{\text{eff}}bt^2} \quad (\mu\varepsilon) \tag{15}$$

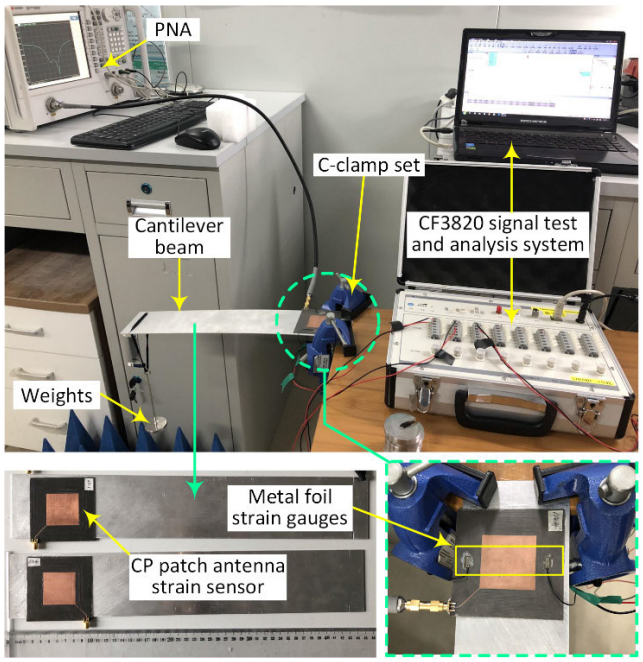

FIGURE 7. Experimental set up of simultaneous measurement of directional strain and input admittance.

where $\boldsymbol{F}$ (= mg) is the directional force in unit of N exerted by weights, L is the length of the cantilever beam, k represents the distance between the center of sensor and the fixed end, b and t are the width and thickness. E_{eff} is the effective elastic modulus of the aluminum plate with a determined value of 50 GPa.

The photographs of the sensors mounted on the cantilever beams and the experimental set up of simultaneous measurement of strain and input admittance are illustrated in Fig. 7, wherein one side of the specimen was fixed to the work bench using C-clamp whereas the other side was loaded progressively using a series of load-weights to stimulate strain levels. The weight-strain conversion can be estimated using the theoretical model (15). The force applied by a set of weights with an increment of 100 g was configured such that a strain increment of 242$\mu\varepsilon$ was obtained. Meanwhile, two metal foil strain gauges were attached onto the patch sensor across the center-line. The data acquisition system (CF3820, Cheng Fu Electronics, China) was used for collecting strain values. The weights applied at the free end are limited at 700 g in order to keep the aluminum beam to operate within its elastic region. Upon each load application, the input admittance of the patch sensor was measured and recorded by the PNA while the strain was measured simultaneously. To minimize the oscillation caused by load change, each PNA and strain measurement took place at least about 30 seconds after the weight change. Note that the compressive strains were measured by upside-downing the cantilever beam with the patch facing downward. In order to examine the system reliability and reduce the random errors in the measuring process, ten cycles of simultaneous measurement were undertaken for each uniaxial scenario. Their average values and standard deviations were used for sensitivities calculation.

C. RESULTS AND DISCUSSION

The average values of input admittance versus frequency under different (average) strain levels for different directions are displayed in Fig. 8. As agreed with prediction results by electromagnetic simulation described in III-C, the frequency shifts of the TM01 mode's maximum admittance determines the x-direction tensile and compressive strain that occurs as shown in Figs. 8(a) and 8(b), respectively, whereas the shifts of TM10 mode's maximum admittance indicates the y-direction strain as shown in Figs. 8(c) and 8(d). Similar observations to simulation results are followed when the patch sensor experiences directional strain. Namely, the TM10 mode's admittance shifts left when the tensile strain increases, conversely, it shifts right when the compressive strain increases. Moreover, there is a significant shift on the minimum between the maxima of two modes, which varies with strain increment. As x-direction tensile strain increases, the minimum admittance increases, and conversely decreases when x-direction compressive strain increases. As predicted, the minimum changes with opposite ways for the y-direction strains, which corroborated with the simulation results as shown in Fig. 3. Therefore, the mode and minimum changes can be used for directional strain detection.

After extracting the minima from the admittance curves at all strain levels from the simulation and experiment, normalization was then performed by dividing the reference minimum admittance. Table 1 lists all average normalized change of admittance $\Delta|\mathrm{Y}|_{\min}$ with standard deviations (STDs) under different strain levels from measurement. Fig. 9 shows the simulated normalized changes of minima-admittance ($\Delta|\mathrm{Y}|_{\min}$) versus the corresponding strain levels, and verified with the experimental results. Both the measured and simulated (minima) data from all strain scenarios underwent a best-straight-line fitting, respectively. The linear functions with goodness-of-fit (R^2) values were shown in the figures. As seen, the fitting curves have good linearity between the changes of normalized $|\mathrm{Y}|_{\min}$ and micro-strain in both the x and y directions as verified by the R^2 values (all>0.997). The simulated linear functions agree with the measured ones from all scenarios. Moreover, very high strain sensitivity factors (in unit of ppm/$\mu\varepsilon$) of the CP-patch sensor were achieved as indicated by the slopes of the linear-fitting curves. Similar sensitivity factors from simulation and measurement were compared and listed in Table 2. It is worthy to mention that the polarity of the admittance-strain sensitivity factors can be used as a verification of direction of strain arisen. Namely, positive value represents a x-direction strain whereas a negative value indicates a y-direction strain. Slight discrepancies were observed, which may be attributed to fabrication and measurement uncertainties. Moreover, a higher strain value may result since the resistive strain gauges were mounted on the substrate rather than the copper patch due to slight strain transfer [20], leading to a lower sensitivity factor. The

TABLE 1. Average measured strain and normalization of Δ|Y|min with standard deviations.

Calculated	X-direction Measurement				Y-direction Measurement			
Strain (με) using (15)	Ave. Strain (με)	Ave. $\Delta\|Y\|_{min}$ (ppm/με)	Strain STD (με)	$\Delta\|Y\|_{min}$ STD (ppm/με)	Ave. Strain (με)	Ave. $\Delta\|Y\|_{min}$ (ppm/με)	Strain STD (με)	$\Delta\|Y\|_{min}$ STD (ppm/με)
-1692	-1635.9	-154333.5	42.7	23909.5	-1608.4	138855.0	31.4	3903.6
-1450	-1422.6	-144994.7	56.4	25111.0	-1397.7	127003.7	31.3	5044.0
-1209	-1132.9	-124860.8	108.3	17885.8	-1175.4	105951.3	25.8	6650.6
-967	-971.5	-101297.0	56.8	9269.6	-951.5	88632.9	22.3	6606.9
-725	-763.9	-76479.7	30.3	13644.8	-721.1	61872.3	14.7	5639.2
-484	-509.6	-52124.7	32.1	8445.7	-486.0	46167.9	6.6	6655.4
-242	-260.5	-30225.8	17.8	5042.8	-223.0	19342.1	74.1	5018.9
0	0.0	0.0	1.5	0.0	0.0	0.0	2.3	0.0
242	243.3	18305.7	23.3	6349.9	234.1	-17907.5	10.5	1892.3
484	486.2	34429.1	28.2	6590.6	468.4	-39526.0	17.0	3626.7
725	738.4	59541.9	23.3	6210.5	705.5	-60787.3	18.6	4029.4
967	950.4	78970.2	78.0	5704.1	943.3	-78742.0	19.0	2162.4
1209	1202.4	98437.8	35.8	5823.2	1175.1	-93462.7	18.8	3697.7
1450	1425.4	114175.5	38.4	5986.9	1404.5	-111452.2	20.4	4716.8
1692	1626.8	135071.7	58.0	4760.7	1609.6	-126211.8	16.3	7079.9

TABLE 2. Wired strain sensitivity factors of CP-patch sensor.

Directional strain	Simulated Sensitivity factor (ppm/με)	Experimental Sensitivity factor (ppm/με)	Discrepancy (%)
x-strain	97.2	91.2	-6.2
y-strain	-99.0	-84.7	-14.4

input admittance of patch sensor is known to be affected if the (metal foil) strain gauges directly attached on top of the patch sensor.

V. A PASSIVE REMOTE SENSING SYSTEM USING CP PATCH-ANTENNA-BASED STRAIN SENSOR

The CP-patch antenna strain transducer can be used in wireless sensing for remote interrogation based on the variation of the radar cross section (RCS/σ) levels read by a radar, e.g. [16], [27], [28]. To illustrate the interrogation method that exploits the input admittance behavior of the proposed CP-patch transducer, the RCS response of the strain sensor is investigated based on the monostatic FMCW radar configurations presented in Fig. 10. In the example of wireless sensing, the CP-patch strain sensor is treated as a load and connected to a standard horn antenna (LB-340-10) through a delay line, at which its length/delay can be set according to backscattering level.

The sensing horn antenna operates in the band of 2.2 GHz to 3.3 GHz with a broadside gain of about 11 dBi. By setting the noise floor (NF) at 1 dB and the minimum signal-to-noise ratio (SNR) as 15 dB, the minimum detectable power of the radar system can be expressed as [27]

$$P_{\min} = kTB\,(NF)\,(SNR) \tag{16a}$$

where k is the Blotzmann's constant, 1.38 × 10.23 J/K, T is temperature 290K, and B is the receiver bandwidth, set at 50 MHz. The radar (transmitting) and sensing antennas are collocated at a maximum interrogation range ($R_{\max}$) when the receiver picks up $P_{\min}$, as given by [35]

$$R_{\max} = \sqrt[4]{\frac{\sigma P_T \lambda^2 G_{0T} \cdot G_{0R}}{(4\pi)^3 P_{min}}} \tag{16b}$$

where G_{0T} and G_{0R} are the maximum broadside gains of the transmitting and sensing antenna, respectively; λ is the free-space wavelength at the center frequency of 2.475 GHz. By taking the antennas imperfections into account, the receiving power in terms of RCS (σ) can be generalized as

$$P_R = \sigma P_T \lambda^2 \frac{G_{0T}\left(1-\Gamma_T^2\right)\cdot G_{0R}\left(1-\Gamma_R^2\right)}{(4\pi)^3 R^4} M_A M_P \tag{16c}$$

where Γ_T and Γ_R are the reflection coefficient of the transmitting and sensing antennas, respectively; M_A and M_P are the displacement loss factor (DLF) and polarization loss factor (PLF), respectively, as given by [35]

$$M_A = DLF = |\cos(\alpha)|^{n*HPBW} \tag{16d}$$

and

$$M_P = PLF = |\cos(\beta)|^2 \tag{16e}$$

where α is the displacement angle between the maximum radiation directions of the two antennas, n (ϵ 0.02, 0.3) is a positive index obtained via curve fitting; whereas β is the angular displacement angle between the radiating apertures.

To understand the transducing mechanism of the CP-patch antenna strain sensor, Fig. 11 displays a graphical relation on the input impedance (expressed on Smith chart), surface current distributions on the copper patch and the complex RCS expressed in polar form under various directional strains. In sequence, the mechanical strain causes the deformation of patch and hence changes the patch's component values (R_{xx}, L_{xx}, C_{xx}) of the orthogonal modes. This then leads to the changes of complex input admittance/impedance as well as the surface current intensity, which finally causes the variation of complex RCS levels.

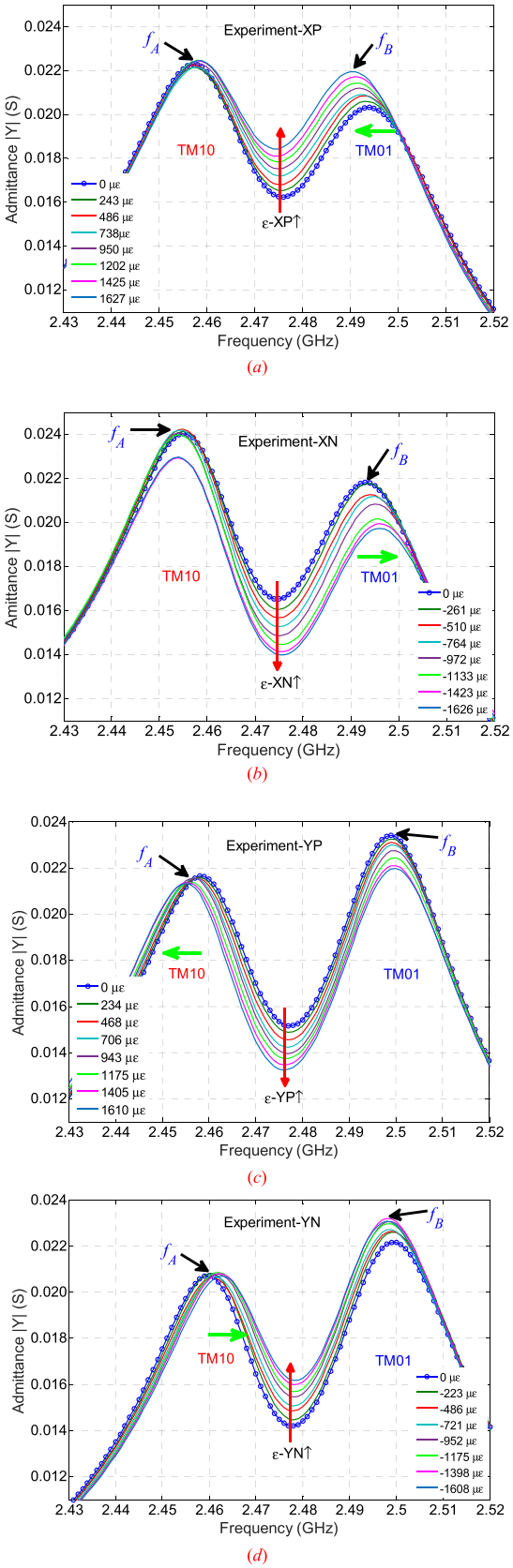

FIGURE 8. Measured input admittance |Y| responses to: (a) x-tensile strain, (b) x-compressive strain, (c) y-tensile strain, and (d) y-compressive strain.

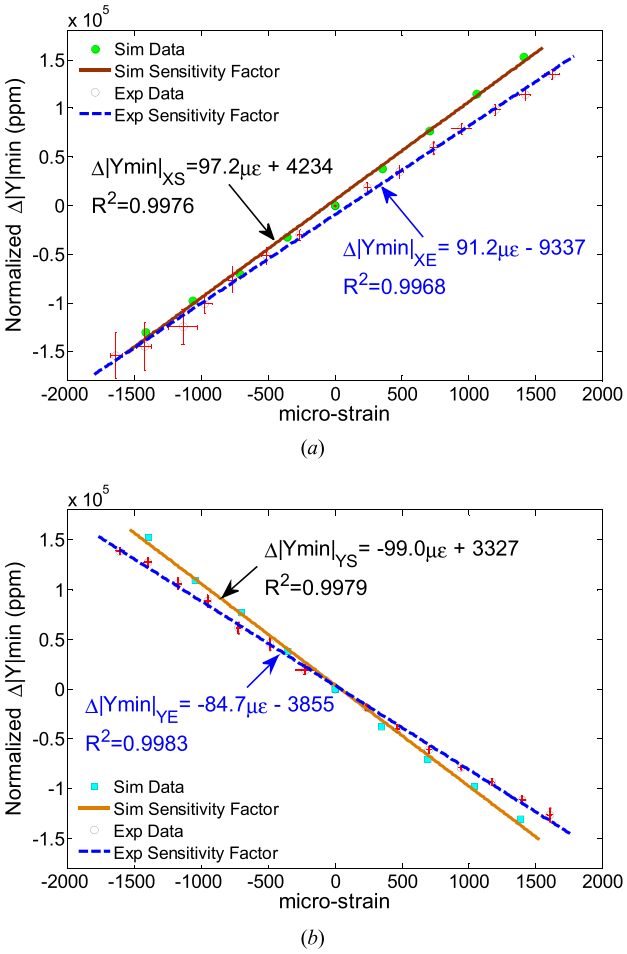

FIGURE 9. Simulated sensitivities compared with measured ones: (a) *x*-strain, (b) *y*- strain.

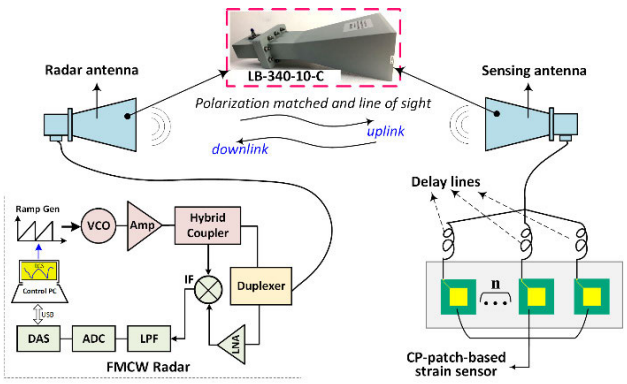

FIGURE 10. Schematic diagram of passive strain sensing based on monostatic radar system.

It should be mentioned that the total RCS (σ) composed of two modes: antenna mode (σ_{an}) and structural mode (σ_{st}). For the structural mode component, the magnitude of the scattered field is due to the structural characteristics (like material, shape and size, etc.) of the sensing antenna and

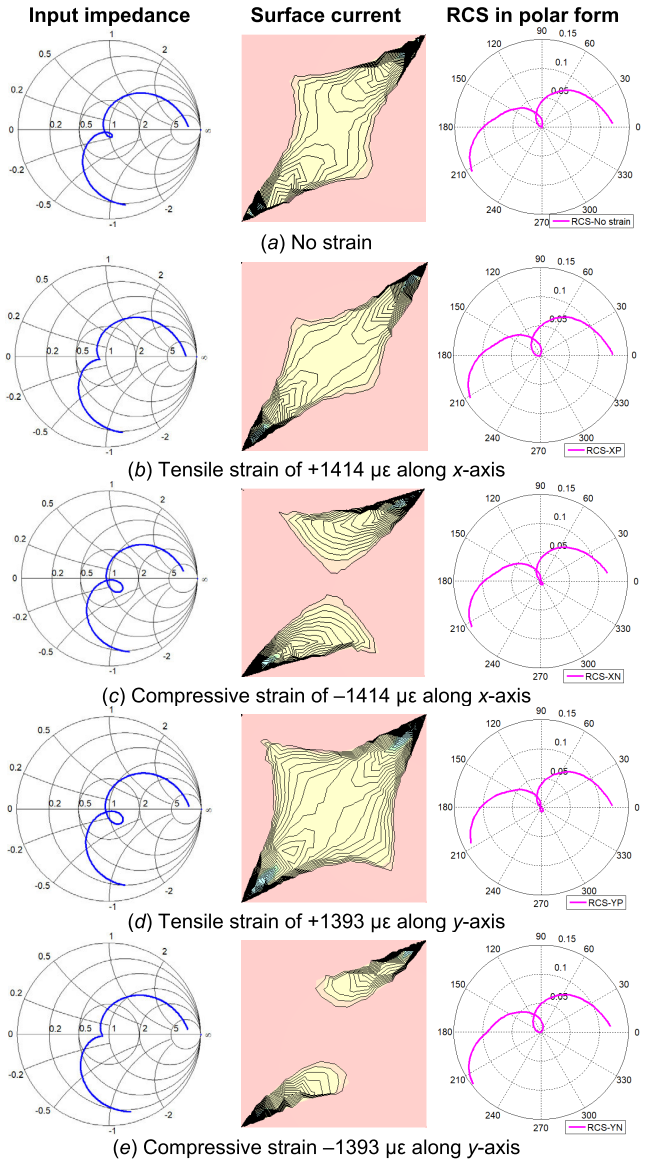

FIGURE 11. Input impedance, surface current distributions (at 2.468 GHz) and the corresponding RCS under extreme strain levels.

is independent of the sensor load, thus being a constant at a narrow bandwidth. The antenna mode is extracted and related to the strain sensing. The antenna mode RCS holds the relationship with the radiation property as given by [35]

$$\sigma_{an} = G(\theta, \varphi)^2 \Gamma_A^2 \frac{\lambda^2}{4\pi}, \tag{17a}$$

where Γ_A is the reflection coefficient of the horn when the CP-patch sensor is connected as a load, and is given by

$$\Gamma_A = \frac{Y_A - Y_L}{Y_A + Y_L} \tag{17b}$$

where Y_A and Y_L are the complex input admittance of the horn antenna and the strain sensor, respectively. The use of S-band high-gain horn antenna pair in the exemplary interrogation system (Fig. 10) may find a disadvantage with its bulky appearance. However, it owns the following advantages in engineering practice over the other methods:

(i) able to realize long-range sensing, over 100 m;
(ii) able to handle large power (P_T) and enhance the signal strength on $RCS_{an}(\sigma_{an})$ with respect to the level of structure mode (σ_{st});
(iii) one sensing antenna is able to flexibly connect with a network of stain sensors via different lengths of delay cable [16], [32];
(iv) sensing element can be arranged away from the sensor's hosting material (e.g. metallic structure [18]). As a result, the backscattering reflects the strain signal with minimal background noise.

The measured data shown from Fig. 8 gives the Y_L together with the input admittance of the sensing horn (Y_A) derive the responses of RCS_{an}, as shown in Fig. 12. There are obvious frequency shifts between two modes (denoted as f_C and f_D) under x-direction strain, as shown in Figs. 12(a) and 12(b). Similarly, frequency shifts of two modes under y-direction strain can be observed as shown in Figs. 12(c) and 12(d). As such, it has clearly not just detected the strain occurrence but also discriminated the strain direction in four scenarios. Moreover, there is a significant change on the maximum of RCS (RCS_{max}) between two modes with strain increment. The RCS_{max} decreases when x-direction tensile strain increases, conversely, it increases when the compressive strain increases. Similarly, opposite movements of maxima are observed for the y-direction strains. Thus the direction of RCS_{max} can be regarded as an indicator for the *bidirectional* strain detection. Consequently, the variations of RCS_{max} offer the feasibility of this interrogation system using CP-patch based strain sensor. Moreover, we took the unique feature of the orthogonal modes of the proposed sensor where the frequencies at which the RCS minima occurred were used as a measurand, namely, $\Delta F = f_D - f_C$. The frequencies f_C and $f_D$shift inward toward the center frequency when tensile strain occurred along the x-direction; conversely, f_C and f_D shift outward when compressive strain arose. However, opposite frequency shifts were observed when the same type of strains followed, respectively, along the y-direction. Based on the RCS data as shown in Fig. 12, we extracted the RCS_{max_ε} as well as the ΔF_ε for each strain level, and their normalized qualities (in ppm) were computed with respect to the reference status as given by

$$\text{Normalized } RCS_{max} = \frac{RCS_{max\_\varepsilon} - RCS_{max\_reference}}{RCS_{max\_reference}} \times 10^6 \tag{18a}$$

$$\text{Normalized } \Delta F = \frac{\Delta F_\varepsilon - \Delta F_{reference}}{\Delta F_{reference}} \times 10^6 \tag{18b}$$

where $RCS_{max\_reference}$ and $\Delta F_{reference}$ are the maximum RCS and frequency difference ΔF under reference status (0 $\mu\varepsilon$).

The corresponding sensitivity factors are obtained by applying curve fitting, as shown in Figs. 13(a) and 13(b), respectively.

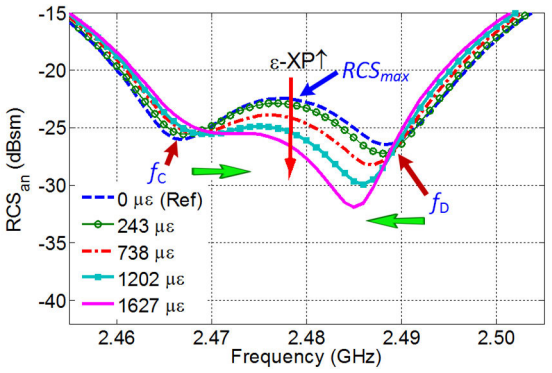

(*a*)

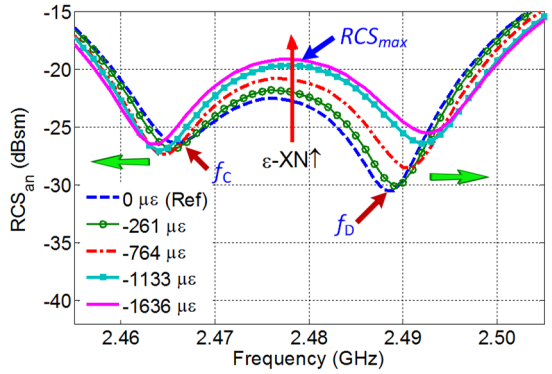

(*b*)

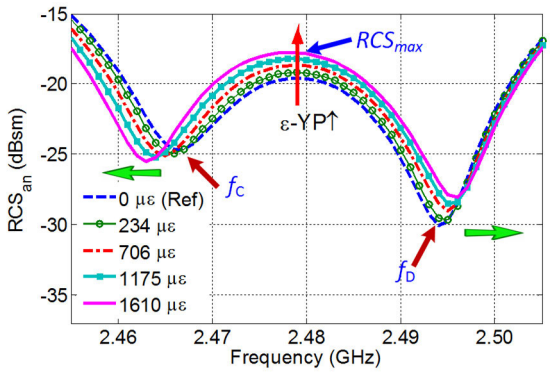

(*c*)

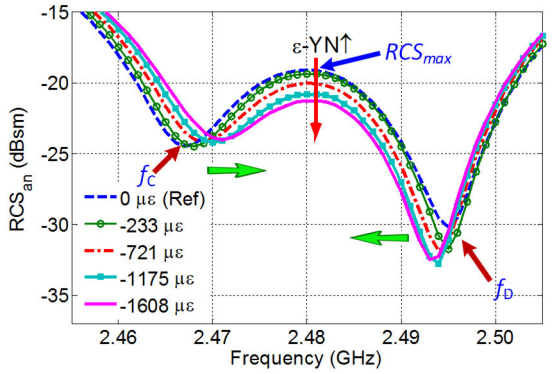

(*d*)

FIGURE 12. Variation of RCSan responses to the strain changes: (a) x-tensile strain, (b) x-compressive, (c) y-tensile, (d) y-compressive strain.

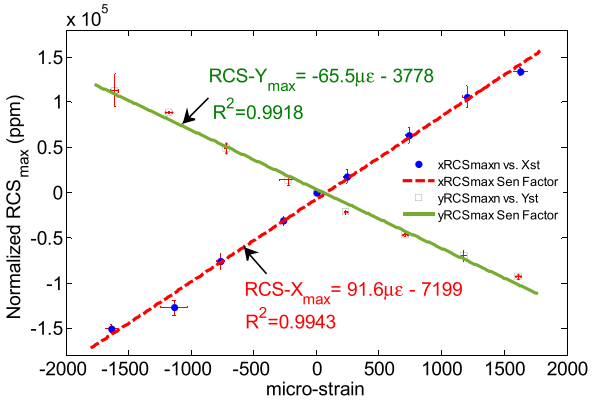

(*a*)

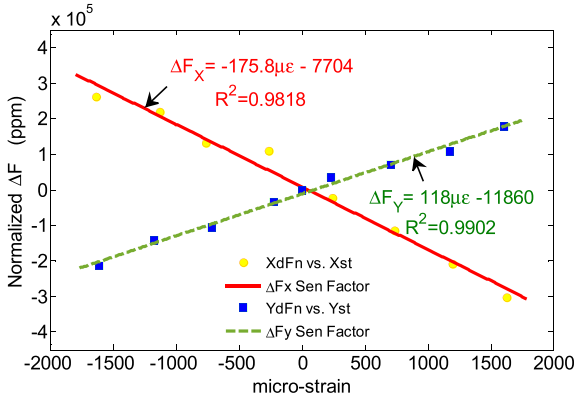

(*b*)

FIGURE 13. Far-field RCS sensitivity factors with strain measurands of (a) maximum RCS, (b) frequency difference ($f_D - f_C$).

TABLE 3. Comparison of sensitivity factors for different types of strain sensors.

Sensor Type	Sensitivity Factor (ppm/με)	Strain direction	Prior strain info
Circular LP-patch sensor [18]	0.2~0.9	multiple	required
Sq. LP-patches with frequency doubling (wireless) [19]	0.91	single	required
Shorted LP-patch sensors [20, [23]-[24]	1 max	orthogonal	required
Metal foil resistive gauge [36]	2	single	required
Single-loop loaded strain transducer [16]	2.35	orthogonal	required
Fabry-Perot interferometer strain sensor [37]	56.7	single	required
Fabric embroidered dipole sensor (wireless, RCS) [38]	0.66	single	required
CP-patch (wire, Y_{min})	85–91	**multiple**	**not required**
CP-patch (wireless, RCS_{max})	65–92		
CP-patch (wireless, RCS: ΔF)	118–176		

A summary of the different types of strain sensors and the theoretical upper bound of sensitivity factors are listed in Table 3. As seen, the CP-patch sensor offers higher sensitivity factor in the order of about 100 times than the LP-patch sensors and 50 times than the traditional metal-foil strain gauges. To the best knowledge of the authors, this is the

highest sensitivity factor of wired RF/microwave strain sensors reported in literature. For far-field (wireless) operation, the proposed sensor in conjunction with the suggested monostatic radar interrogation system can offer a sensitivity factor as high as 176 ppm/$\mu\varepsilon$ (Fig. 13(*b*)). In addition, the proposed CP-patch strain sensor owns the advantage that *a priori* strain information (e.g. strain direction) is not required and can be used for multidirectional strain monitoring. A single CP-patch sensor can replace two LP-patch sensors for simultaneous detection of orthogonal strains. Ultimately, it saves the system cost of 50% or more as compared with the use of LP-patch sensors. The frequency method is known to be better, with less noise and interference susceptibility than the amplitude method during the wireless interrogation. The proposed CP-patch sensor with the exemplary wireless interrogation system offers multiple measurands: ΔF and RCS_{max}. Nevertheless, the use of frequency difference between two modes as the strain measurand may give advantages such as low cost and reliability as compared to use of RCS amplitude.

VI. CONCLUSION

An innovative design of a highly sensitive strain sensor is introduced in this paper. Our study takes a step forward from the LP patch-based strain sensors to the single-feed CP patch sensor that cater for multidirectional strain monitoring over metallic surfaces. The newly proposed evaluation method of minima-admittance, rather than the resonant frequency method, have been illustrated and successfully validated through simulation with experimental results. This new idea also enables a new dimension of sensitivity factor in this type of strain sensing which was previously limited to the linear scale of the changes in the dimensions of the structures. By utilizing the two orthogonal modes' admittance, the prototypes give a sensitivity factor of around 90 ppm/$\mu\varepsilon$ under wire and 176 ppm/$\mu\varepsilon$ under wireless condition, which are much higher than traditional strain gauges and the existing LP-patch or other resonator sensors using resonant frequency as evaluation parameter. This work also illustrates feasibility for measurements of strain vector field of metallic surfaces, and the design is also the first of its kind to be accessible of multidirectional strain sensing. Although results were not directly measured, direct deduction from the decomposition of forces could be feasible by using strain sensor of this type. Therefore, the proposed sensor can be an outstanding alternative for traditional strain gages because one CP-patch sensor is able to detect multidirectional strain in one plane whereas traditional strain gauge requires multiple sensing elements. With the well advanced RCS and signal processing technologies and the simplicity of the design, a remote strain detecting method can be readily obtained. Apart from the RCS detection architecture, the sensing element and its working principles can be easily scaled to operate at millimeter-wave frequencies for higher resolution of strain sensing or adapted to biomedical applications at lower frequencies.

REFERENCES

[1] D. Balageas, *Structural Health Monitoring*, 1st ed. London, U.K.: ISTE Ltd, 2006, pp. 15–64.
[2] D. Kujawski and F. Ellyin, "A fatigue crack propagation model," *Eng. Fracture Mech.*, vol. 20, pp. 695–704, Jan. 1984.
[3] A. M. Mahmoud, H. H. Ammar, O. M. Mukdadi, I. Ray, F. S. Imani, and A. Chen, "Non-destructive ultrasonic evaluation of CFRP-concrete specimens subjected to accelerated aging conditions," *NDT E Int.*, vol. 40, no. 7, pp. 635–664, Jun. 2010.
[4] Z. Lu, C. Hong, Y. Zhang, D. Su, and Y. Fu, "Development of an FBG sensor for measuring large range and multi-directional settlement," *IEEE Access*, vol. 7, pp. 107669–107677, Aug. 2019.
[5] A. K. Singh, S. Berggren, Y. Zhu, M. Han, and H. Huang, "Simultaneous strain and temperature measurement using a single fiber Bragg grating embedded in a composite laminate," *Smart Mater. Struct.*, vol. 26, no. 11, pp. 115025–115034, Nov. 2017.
[6] T. T. Pham, H. Zhang, S. Yenuganti, S. Kaluvan, and J. A. Kosinski, "Design, modeling, and experiment of a piezoelectric pressure sensor based on a thickness-shear-mode crystal resonator," *IEEE Trans. Ind. Electron.*, vol. 64, no. 11, pp. 8484–8491, Nov. 2017.
[7] J. Fu, Y. Guo, and P. Li, "A fiber Bragg grating anchor rod force sensor for accurate anchoring force measuring," *IEEE Access*, vol. 8, pp. 12796–12801, Jan. 2020.
[8] H. Xia, Y. Xia, Y. Ye, L. Qian, and G. Shi, "Simultaneous wireless strain sensing and energy harvesting from multiple piezo-patches for structural health monitoring applications," *IEEE Trans. Ind. Electron.*, vol. 66, no. 10, pp. 8235–8243, Oct. 2019.
[9] A. Oliveri, M. Maselli, M. Lodi, M. Storace, and M. Cianchetti, "Model-based compensation of rate-dependent hysteresis in a piezoresistive strain sensor," *IEEE Trans. Ind. Electron.*, vol. 66, no. 10, pp. 8205–8213, Oct. 2019.
[10] L. Da Xu, W. He, and S. Li, "Internet of Things in industries: A survey," *IEEE Trans. Ind. Informat.*, vol. 10, no. 4, pp. 2233–2243, Nov. 2014.
[11] C. Arcadius Tokognon, B. Gao, G. Y. Tian, and Y. Yan, "Structural health monitoring framework based on Internet of Things: A survey," *IEEE Internet Things J.*, vol. 4, no. 3, pp. 619–635, Jun. 2017.
[12] Z. Shao, X. Zhang, Y. Li, and J. Jiang, "A comparative study on radar interferometry for vibrations monitoring on different types of bridges," *IEEE Access*, vol. 6, pp. 29677–29684, Jun. 2018.
[13] J. Zhang, G. Tian, A. Marindra, A. Sunny, and A. Zhao, "A review of passive RFID tag antenna-based sensors and systems for structural health monitoring applications," *Sensors*, vol. 17, no. 2, pp. 265–297, 2017.
[14] S. Deif and M. Daneshmand, "Multiresonant chipless RFID array system for coating defect detection and corrosion prediction," *IEEE Trans. Ind. Electron.*, vol. 67, no. 10, pp. 8868–8877, Oct. 2020.
[15] A. M. J. Marindra and G. Y. Tian, "Chipless RFID sensor tag for metal crack detection and characterization," *IEEE Trans. Microw. Theory Techn.*, vol. 66, no. 5, pp. 2452–2462, May 2018, doi: 10.1109/TMTT.2017.2786696.
[16] T. T. Thai, H. Aubert, P. Pons, G. DeJean, M. M. Tentzeris, and R. Plana, "Novel design of a highly sensitive RF strain transducer for passive and remote sensing in two dimensions," *IEEE Trans. Microw. Theory Techn.*, vol. 61, no. 3, pp. 1385–1396, Mar. 2013.
[17] U. Tata, S. Deshmukh, J. C. Chiao, R. Carter, and H. Huang, "Bio-inspired sensor skins for structural health monitoring," *Smart Mater. Struct.*, vol. 18, no. 10, pp. 104026–204033, Oct. 2009.
[18] A. Daliri, A. Galehdar, S. John, C. H. Wang, W. S. T. Rowe, and K. Ghorbani, "Wireless strain measurement using circular microstrip patch antennas," *Sens. Actuators A, Phys.*, vol. 184, pp. 86–92, Sep. 2012.
[19] C. Cho, X. Yi, D. Li, Y. Wang, and M. M. Tentzeris, "Passive wireless frequency doubling antenna sensor for strain and crack sensing," *IEEE Sensors J.*, vol. 16, no. 14, pp. 5725–5733, Jul. 2016.
[20] X. Yi, T. Wu, Y. Wang, R. T. Leon, M. M. Tentzeris, and G. Lantz, "Passive wireless smart-skin sensor using RFID-based folded patch antennas," *Int. J. Smart Nano Mater.*, vol. 2, no. 1, pp. 22–38, Feb. 2011.
[21] X. H. Yi, C. Cho, J. Cooper, Y. Wang, M. M. Tentzeris, and R. T. Leon, "Passive wireless antenna sensor for strain and crack sensing-electromagnetic modeling, simulation, and testing," *Smart Mater. Struct.*, vol. 22, no. 8, pp. 085009–085025, Aug. 2013.
[22] X. Yi, C. Cho, Y. Wang, and M. M. Tentzeris, "Battery-free slotted patch antenna sensor for wireless strain and crack monitoring," *Smart Struct. Syst.*, vol. 18, no. 6, pp. 1217–1231, Dec. 2016.

[23] S. C. Wang and M. S. Tong, "Mechanical deformation detection of building structures using microstrip patch antennas as sensors," *IEEE Sensors J.*, vol. 18, no. 21, pp. 8684–8876, Nov. 2018.
[24] X. Yi, T. Wu, Y. Wang, and M. M. Tentzeris, "Sensitivity modeling of an RFID-based strain-sensing antenna with dielectric constant change," *IEEE Sensors J.*, vol. 15, no. 11, pp. 6147–6155, Nov. 2015.
[25] X. Xu and H. Y. Huang, "Multiplexing passive wireless antenna sensors for multi-site crack detection and monitoring," *Smart Mater. Struct.*, vol. 21, no. 1, pp. 015004–015012, Jan. 2012.
[26] J. Zhang, B. Huang, G. Zhang, and G. Y. Tian, "Wireless passive ultra-high frequency RFID antenna sensor for surface crack monitoring and quantitative analysis," *Sensors*, vol. 18, no. 7, pp. 2130–2140, Jul. 2018.
[27] D. J. Thomson, D. Card, and G. E. Bridges, "RF cavity passive wireless sensors with time-domain gating-based interrogation for SHM of civil structures," *IEEE Sensors J.*, vol. 9, no. 11, pp. 1430–1438, Nov. 2009, doi: 10.1109/JSEN.2009.2027407.
[28] J. Yao, S. Tjuatja, and H. Huang, "Real-time vibratory strain sensing using passive wireless antenna sensor," *IEEE Sensors J.*, vol. 15, no. 8, pp. 4338–4345, Aug. 2015.
[29] H. Cheng, S. Ebadi, and X. Gong, "A low-profile wireless passive temperature sensor using resonator/antenna integration up to 1000°C," *IEEE Antennas Wireless Propag. Lett.*, vol. 11, pp. 369–372, Apr. 2012.
[30] J.-M. Boccard, T. Aftab, J. Hoppe, A. Yousaf, R. Hutter, and L. M. Reindl, "High-resolution, far-field, and passive temperature sensing up to 700°C using an isolated ZST microwave dielectric resonator," *IEEE Sensors J.*, vol. 16, no. 3, pp. 715–722, Feb. 2016.
[31] J. Yao, F. Mbanya Tchafa, A. Jain, S. Tjuatja, and H. Huang, "Far-field interrogation of microstrip patch antenna for temperature sensing without electronics," *IEEE Sensors J.*, vol. 16, no. 19, pp. 7053–7060, Oct. 2016.
[32] D. Girbau, A. Ramos, A. Lazaro, S. Rima, and R. Villarino, "Passive wireless temperature sensor based on time-coded UWB chipless RFID tags," *IEEE Trans. Microw. Theory Techn.*, vol. 60, no. 11, pp. 3623–3632, Nov. 2012.
[33] K. L. Chung, L. Wang, J. Luo, Y. Li, and Y. Li, "Comparative study on directional sensitivity of patch-antenna-based strain sensors," *Int. J. RF Microw. Comput.-Aided Eng.*, vol. 30, no. 11, Aug. 2020, doi: 10.1002/mmce.22398.
[34] R. Garg, P. Bhartia, I. Bahl, and A. Ittipiboon, *Microstrip Antenna Design Handbook*. Boston, MA, USA: Artech House, 2001.
[35] W. L. Stutzman, and G. A. Thiele, *Antenna Theory and Design*, 3rd ed., Hoboken, NJ, USA: Wiley, 2012.
[36] M. Bao, *Analysis and Design Principles of MEMS Devices*. Amsterdam, The Netherlands: Elsevier, Dec. 2014, ch. 1.
[37] K. Zhou, M. Z. Ai, Z. H. Qian, X. X. Gao, and Z. H. Hu, "High-sensitivity strain sensor with an in-fiber air-bubble Fabry–Pérot interferometer," *Appl. Phys. Lett.*, vol. 113, no. 18, pp. 181901–191905, Oct. 2018, doi: 10.1063/1.5058200.
[38] M. Hasani, A. Vena, L. Sydanheimo, L. Ukkonen, and M. M. Tentzeris, "Implementation of a dual-interrogation-mode embroidered RFID-enabled strain sensor," *IEEE Antennas Wireless Propag. Lett.*, vol. 12, pp. 1272–1275, Sep. 2013, doi: 10.1109/LAWP.2013.2283539.